

# A Stretchable and Highly Sensitive Graphene-Based Fiber for Sensing Tensile Strain, Bending, and Torsion

Yin Cheng, Ranran Wang,\* Jing Sun,\* and Lian Gao

Wearable sensors, devised to capture and monitor various human activities, have attracted great attention due to the fascinating efficacy, and also achieved considerable progress along with the development of flexible and stretchable electronics.<sup>[1–10]</sup> Conventional strain gauges, based on metal foils and semiconductors, are apparently incompetent to be utilized as sensing components in wearable sensing, limited by their poor mechanical compliance and low workable range (<5% strain).<sup>[11,12]</sup> Nanomaterials with excellent nanoscale flexibility and electrical properties have been frequently employed in flexible strain sensors, such as carbon nanotubes (CNTs),<sup>[1,3,6,13,14]</sup> graphene,<sup>[15–23]</sup> and metallic nanowires.<sup>[24,25]</sup> Despite the high performance of these devices, there still exist two constraints that restrict the widespread application. On the one hand, it seems a dilemma to attain the combination of high sensitivity to tiny deformation and broad sensing range, which is of crucial importance to realize the detection of full-range human activities, ranging from physiological signals as subtle as heart-beat and breathing, to human motions as vigorous as finger-bending and running. On the other hand, vast majority of the reported sensors are of single function, incapable of sensing multiple forms of mechanical deformations, thus unfavorably hindering the detection of complex human body movements involving tensile strain, bending, and twisting.

Here, we develop a facile, low-cost, and scalable fabricating strategy for graphene-based composite fiber with “compression spring” architecture. This composite fiber exhibits an incorporation of ultrahigh sensitivity to tensile strain deformation (detection limit of 0.2% strain) and wide maximal sensing range (up to 100% strain). Besides, fast signal response (<100 ms) and high reproducibility (up to 10 000 cycles) were observed. Furthermore, except as a strain sensor, the fiber sensor also possesses excellent bending- and torsion-sensitive properties due to the microstructure variation under different mechanical stimuli. We integrated the graphene-based fibers into wearable sensors and succeeded in detecting full-range human activities, from as subtle as accurate speech recognition, sleep quality evaluation, pulse monitoring, to vigorous human motions (such as walking, jogging, and jumping) capturing. We also expand the application to real-time monitoring

and recording of complex robot movements, for example, the “Gangnam Style” dance.

Figure 1a–d shows the schematic illustration of the fabrication strategy of the fiber sensor and the scanning electron microscopy (SEM) images of the fiber sample during the whole process (see the Experimental Section for fabrication details and Figure S1–S4 in the Supporting Information for detailed SEM results). A double-covered yarn, composed of a highly elastic polyurethane (PU) core fiber and polyester (PE) fibers winding around helically, served as the elastic scaffold (Figure 1a and Figure S5, Supporting Information). After air plasma treatment, the fiber was etched (designated as PDCY), creating ripple-like texture (Figure S2, Supporting Information) on PE fibers, and gained a considerable improvement of hydrophilicity owing to the generation of oxygen-containing polar groups (Figure 1b and Figure S6, Supporting Information).<sup>[26]</sup> Afterward, the PDCY was dip-coated with graphene oxide (GO) (PDCY–GO; Figure S7, Supporting Information).<sup>[27]</sup> The GO sheets wrapped on the surface of PE fibers conformally, thus leaving the ripple texture still clearly visible (Figure 1c and Figure S3, Supporting Information). Lastly the PDCY–GO was soaked in hydriodic (HI) acid to obtain a reduced GO (RGO) coated fiber (PDCY–RGO; Figure 1d and Figure S4, Supporting Information).<sup>[28]</sup> Figure 1e presents the micro-Raman spectra at PE fiber surface of PDCY, PDCY–GO (2 dip-coating times), and PDCY–RGO (2 and 6 dip-coating times). The  $I_D/I_G$  ratio increased (0.92 to 1.26) from PDCY–GO (2) to PDCY–RGO (2), indicating the decrease in the average size of the  $sp^2$  domains and increase in quantities of structural defects,<sup>[29]</sup> confirming the efficient reduction of GO to RGO. The as-prepared fibers were light-weighted ( $0.28 \text{ g m}^{-1}$ ) and flexible enough to conform to arbitrary curved surfaces (inset in Figure 1f, winding around a finger). For the fibers dip-coated from two to six times, the resistance along the fiber axis was found to be highly linearly proportional to the length (Figure S8, Supporting Information), implying uniform coating of GO in the dip-coating process. The electrical conductivity of the composite fiber increased from  $0.012$  to  $0.136 \text{ S m}^{-1}$  along with the dip-coating times from 2 to 6 (Figure 1f, see the Supporting Information for detailed measurement and calculation). We evaluated the mechanical properties of DCY and PDCY–RGO (2) using tensile stress versus strain measurements (Figure 1g). The rupture strain for DCY and PDCY–RGO (2) reached up to 656% and 676%, the tensile strength being 29.01 and 29.14 MPa, respectively. An ultrasonic test proved a solid adsorption of RGO on the polymer surface (Figure S9, Supporting Information). Noteworthy is that the electrical resistance of graphene-based fibers maintained stability in ambient environment (Figure S10, Supporting Information).

To investigate the strain sensing properties, the relative resistance variation ( $\Delta R/R_0$ ) was traced under various strain loading

Dr. Y. Cheng, R. Wang, Prof. J. Sun, L. Gao  
State Key Laboratory of High Performance  
Ceramics and Superfine Microstructure  
Shanghai Institute of Ceramics  
Chinese Academy of Sciences  
Shanghai 200050, China  
E-mail: wangranran@mail.sic.ac.cn;  
jingsun@mail.sic.ac.cn



DOI: 10.1002/adma.201503558

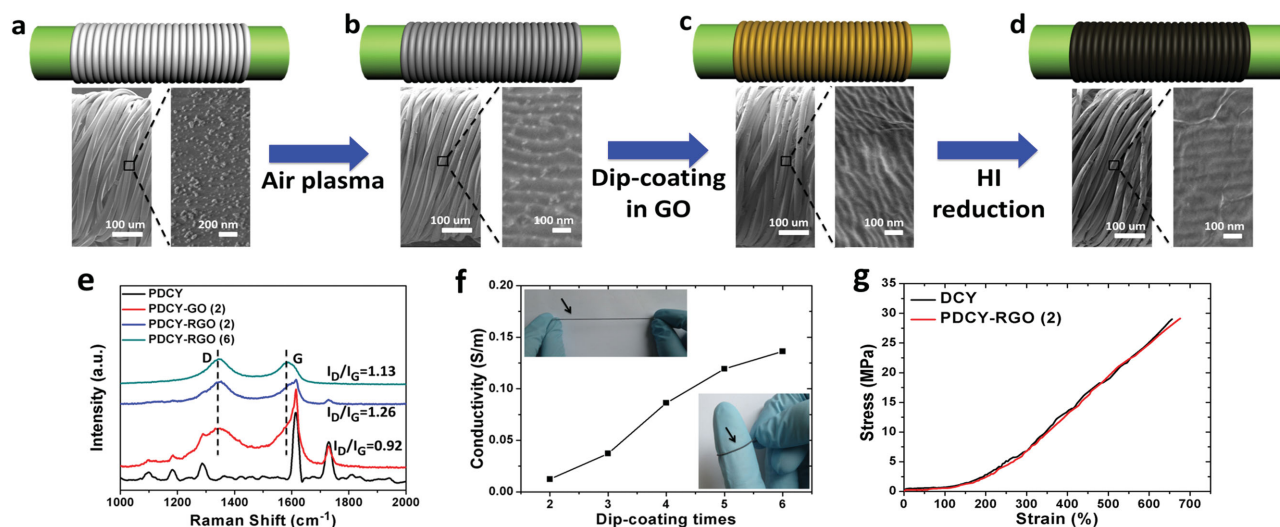


**Figure 1.** Schematic illustration of the fabrication process and the characterization of the graphene-based fiber. a–d) Fabrication process of the graphene-based fiber. a) Schematic structure of DCY and SEM images of DCY and PE fiber surface (for simplicity and clarity, only one layer of PE fibers was demonstrated in the structural drawing). b) Schematic structure of PDCY and SEM images of PDCY and PE fiber surface after air plasma treatment. c) Schematic structure of PDCY–GO and SEM images of PDCY–GO (2 dip-coating times) and PE fiber surface after GO coating. d) Schematic structure of PDCY–RGO (2 dip-coating times) and PE fiber surface after HI reduction. e) Micro-Raman spectra of PDCY (black line), PDCY–GO of 2 dip-coating times (blue line), and PDCY–RGO of 6 dip-coating times (green line). f) Electrical conductivity of PDCY–RGO at varying dip-coating times. Upper-left photograph shows the as-prepared graphene-based fiber (pointed out by a black arrow). The lower-right photograph demonstrates the graphene-based fiber winding around a finger with ease. g) Stress versus strain curves of DCY and PDCY–RGO (2 dip-coating times).

conditions by maintaining constant voltage across the sensor device. **Figure 2a** illustrates the resistance variation of graphene-based fibers with varying dip-coating times under tensile strain. For all the samples, resistance increased monotonically with tensile strain up to 100% and then leveled off to strain of 200%. We noticed that within 50% strain, the graphene-based fiber sensors with varying dip-coating times presented highly coincident  $\Delta R/R_0 \gg$  strain curves (inset in **Figure 2a**). The fiber of 2 dip-coating times was chosen as the testing sample in the later sections, unless otherwise specified. **Figure 2b** depicts the resistance variation of a 50% strain stretching–releasing cycle. Gauge factor (GF), defined as  $(\Delta R/R_0)/\epsilon$ , where  $\epsilon$  is the strain, is the representative parameter to assess sensitivity. From the stretching curve in **Figure 2b**, the averaged GF was calculated (Table S1, Supporting Information). The averaged GF was 10 within 1% strain and 3.7 within 50% strain, endowing the sensor with a desirable combination of high sensitivity at small strain and broad sensing range, which greatly expands its application in daily life, especially as a full-range human motion sensor. Yamada et al. assembled aligned single-walled carbon nanotube (SWCNT) films onto poly(dimethylsiloxane) (PDMS) substrate as wearable sensors for human-motion detection.<sup>[3]</sup> This strain sensor was capable of measuring strains up to 280%, making it qualified to detect relatively drastic motions, such as finger-bending and walking. However, its low GF (0.82 within 40% strain and 0.06 from 60% to 200% strain) restricted the detection of slight physiological signals, such as pulse and precise speech recognition. Graphene woven fabrics (GWFs) on PDMS have been exploited as wearable sensors. The ultra-high GF (35 at 0.2% strain) enabled the device to monitor subtle motions such as clench, breathing, and even pluse.<sup>[16,21]</sup> Nevertheless, the small working range ( $\gg 10\%$ ) rendered it

incompetent to accommodate intense exercise such as running, jumping, squatting, and so on. Recently, a graphene–rubber composite was utilized as fiber sensor with high sensitivity (GF up to 35) and high strain rate (exceeding 6000% per second), which was particularly suitable for bodily motion sensing.<sup>[18]</sup>

The detection limit of the fiber sensor was determined by applying gradually diminishing step strain (**Figure 2c**). Benefiting from the high sensitivity at small strain range, the detection limit could be as minute as 0.2%, and the output signal was highly reproducible at minute strains (inset in **Figure 2c** and **Figure S11**, Supporting Information), accompanied by a superb signal stability for long-time step-strain input even at minimal strains (**Figure S12** and **Table S2**, Supporting Information).

In addition to high sensitivity and wide sensing range, the fiber sensor also has important advantages of low creep and fast response. As seen in **Figure 2d**, a step strain of 10% was imposed, revealing a percent overshoot and creep recovery time of 3.3% and 3 s, respectively (see Supporting Information **Figure S13** for larger step strains). These compare favorably<sup>[3]</sup> or far better<sup>[30]</sup> than some reported results. To determine the response time, the sensor was loaded with a quasi-transient step strain of 0.5% (see the Supporting Information for details). With the assistance of the real-time high-resolution  $I$ – $t$  response curve (**Figure 2e**), the response time was determined to be less than 100 ms. The fast response undoubtedly facilitates the real-time monitoring of fast and intricate movements, such as dancing. Durability and stability are extremely critical for practical application. Multiple loading cycles (30% and 50% strain for sensors 1 and 2, respectively) were performed (**Figure 2f**). The response signal remained nearly unchanged after 1000 cycles for both sensors 1 and 2. After 10 000 cycles, the relative signal drifts at maximal strains (30% and 50%, respectively) of sensors 1 and 2

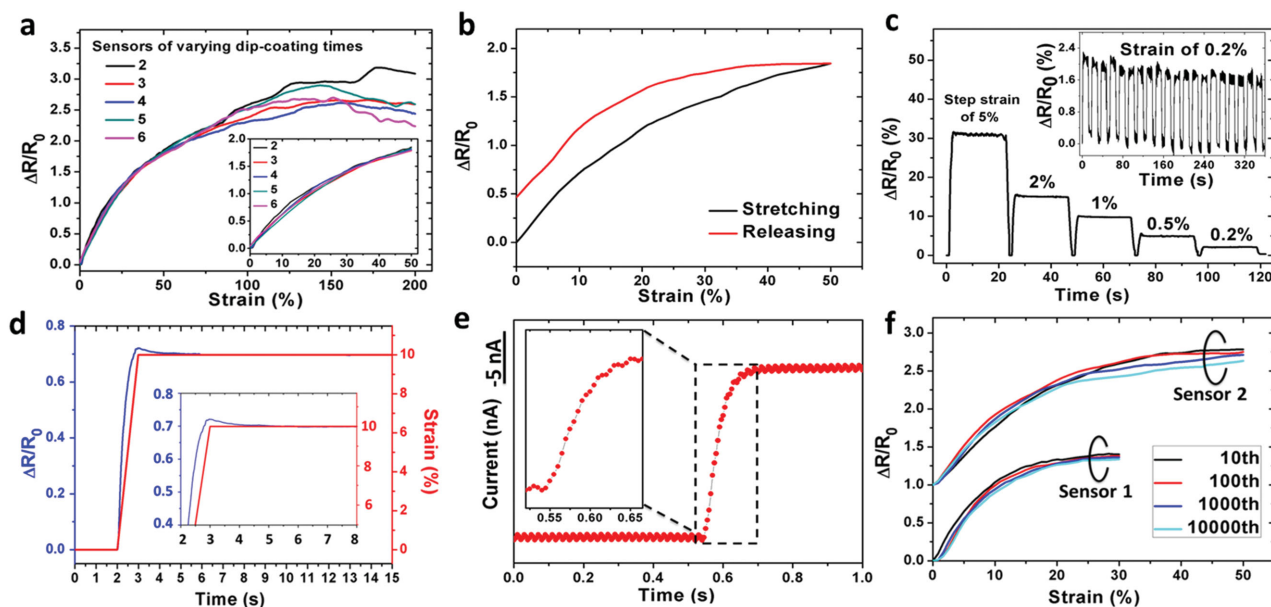


**Figure 2.** Strain sensing properties of the graphene-based fiber. a) Relative resistance variation of graphene-based fibers with varying dip-coating times (two to six times) when being stretched (strain rate of 50% per minute) up to 200% strain. The inset reproduces the curves within 0–50% strain range. b) Resistance variation under a 50% strain stretching-releasing cycle. c) Resistance variation under gradually diminishing step strain from 5% to 0.2% strain. The inset shows the response signal at 20 consecutive input step strain of 0.2%. d) Resistance variation at a step strain of 10% (strain rate of 10%/s). Inset: Closeup of the overshoot. e) Current signal of the fiber sensor to a quasi-transient input step strain of 0.5% (see the Supporting Information for details). Inset: Closeup of the response time (resolution limit of 5 ms). f) Resistance variation for multiple-cycle tests: 10th (black), 100th (red), 1000th (blue), and 10 000th (cyan) cycles at 0–30% (sensor 1) and 0–50% (sensor 2). The baseline of sensor 2 is raised by 100%. The sample used in strain sensing investigation was 20 mm.

were as small as  $-4.7\%$  and  $-8.6\%$ , respectively (see Supporting Information Table S3 for more details), allowing for the reliable practical utilization as daily wearable sensors. Table S4 (Supporting Information) listed the main performance criteria of typical graphene-based strain sensors as comparison.

To realize the detection of bending, we integrated the graphene-based fiber onto a PDMS slab. The sensor inherited superb flexibility of the PDMS upholder (Figure 3a) and the bending angle  $\theta$  was defined in the inset of Figure 3a. We harnessed the bending-induced strain on the upper surface of the PDMS slab as a stimulus to the graphene-based fiber, which in turn reflected the bending extent (detailed mechanism analysis is given in the Supporting Information). Figure 3b revealed a wide sensing range of bending angle up to  $90^\circ$  and also a repeatable response in forward (bending) and reverse (bending back) directions. Through exerting a series of decreasing step bending angle (inset in Figure 3b and Figure S14, Supporting Information), the detection limit was found to be as tiny as  $2^\circ$  (Figure 3c), also proved to be reproducible and stable (inset in Figure 3c). The outstanding properties in bending sensing enable the fiber sensor to monitor joint bending of humans and robots.

Except tensile strain and bending, torsion is another ubiquitous mechanical deformation, commonly observed in human joints, robotics, and even artificial torsional muscles.<sup>[31]</sup> We here skillfully leveraged the intrinsic twisting microstructure (inset in Figure 3d) of the PE fibers to employ the graphene-based fiber as torsion sensor (detailed mechanism analysis is given in the Supporting Information). The  $\Delta R/R_0$  versus torsion level curve in Figure 3d demonstrated a strikingly wide dynamic range of torsion sensing ( $-280 \text{ rad m}^{-1}$  to  $800 \text{ rad m}^{-1}$ ;

a wider response curve in Figure S15, Supporting Information), superior to conventional optical fiber torsion sensor<sup>[32]</sup> ( $-100 \text{ rad m}^{-1}$  to  $100 \text{ rad m}^{-1}$ ) and aligned SWCNT films-based torsion sensor<sup>[33]</sup> ( $-100 \text{ rad m}^{-1}$  to  $400 \text{ rad m}^{-1}$ ). Furthermore, the sensor was capable of discriminating between counterclockwise (defined as positive torsion) and clockwise (defined as negative torsion) twists via the increase and decrease of the resistance, giving it an advantage over a reported GWF-based torsion sensor.<sup>[34]</sup> Figure 3e recorded the resistance variation during ten cycles of low level torsion (in the counterclockwise direction; see Supporting Information Figure S16 for the clockwise direction), indicating the detection limit could be as low as  $2 \text{ rad m}^{-1}$  with high reproducibility. Figure 3f presented the durability test results of 5000 cyclic torsion ( $-240 \text{ rad m}^{-1}$  to  $500 \text{ rad m}^{-1}$ ). Within the torsion level of  $-200 \text{ rad m}^{-1}$  to  $150 \text{ rad m}^{-1}$ , the resistance variation remained quite stable. At torsion level of  $500 \text{ rad m}^{-1}$ , the signal drifts were 17.7% and 37.4% after 1000 and 5000 cycles, respectively, compared with the 10th cycling. This might be attributed to the abrasion of RGO coating in the twisting process. Lastly, the hysteresis was fairly minimal even at the 5000th torsion cycle (Figure S17, Supporting Information). The excellent features in torsion sensing will enrich the application of the fiber sensor in capturing sophisticated motions. The performance comparison of the typical torsion sensors was listed in Table S5 (Supporting Information).

To understand the mechanism underlying the resistance variation in strain sensing, we traced the microstructure of the fiber from 0% to 50% strain (Figure 4a–c and Figure S18–S21, Supporting Information). The SEM results suggested, in terms of the PE fiber layers, the elongation was accommodated by the



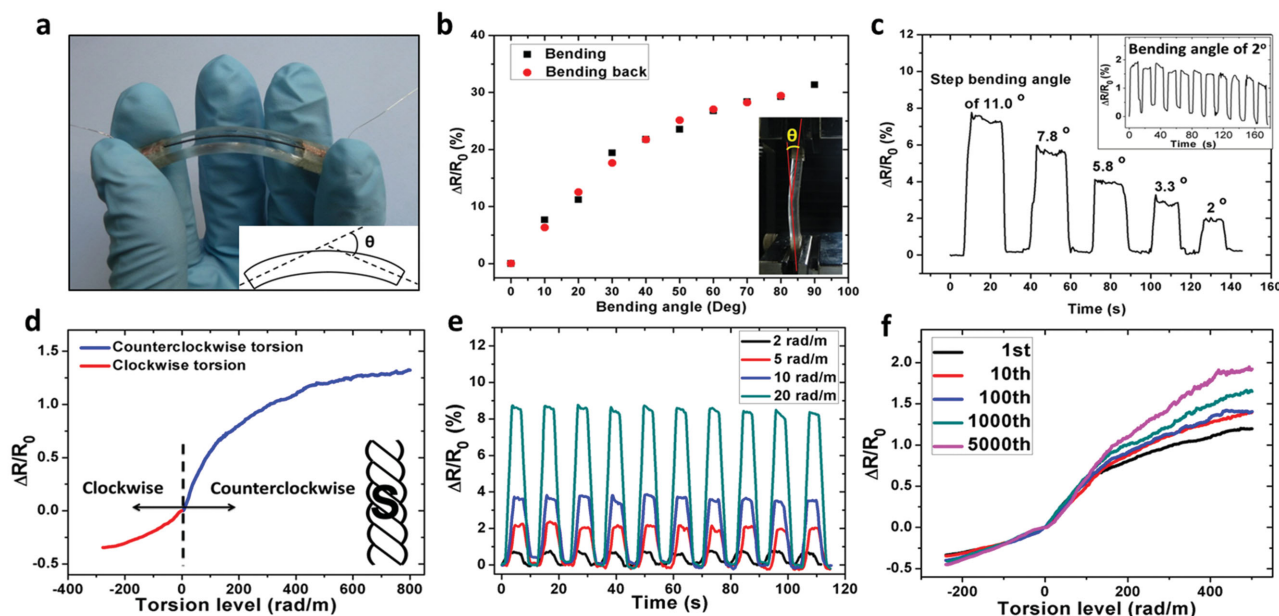


**Figure 3.** Bending and torsion sensing properties of the graphene-based fiber. a) Photograph of the bending sensor. Inset: The definition of bending angle  $\theta$  in a schematic structure. b) Resistance variation of the bending sensor in forward (bending) and reverse (bending back) directions. Inset: Bending sensor in testing. c) Resistance variation of the bending sensor under a series of decreasing step bending angle from  $11.0^\circ$  to  $2^\circ$ . Inset: Resistance variation during ten bending cycles at  $2^\circ$ . d) Resistance variation of the graphene-based fiber in torsion test from  $-280 \text{ rad m}^{-1}$  to  $800 \text{ rad m}^{-1}$ . Inset: Structure drawing of the twisting PE fiber (outer layer of S-twist). e) Resistance variation during ten cycles of low torsion levels from  $20 \text{ rad m}^{-1}$  to  $2 \text{ rad m}^{-1}$  (in the counterclockwise direction; see Figure S16 in the Supporting Information for the clockwise direction). f) Resistance variation in durability test: 1st (black), 10th (red), 100th (blue), 1000th (green), and 5000th (magenta) cycles at  $-240 \text{ rad m}^{-1}$  to  $500 \text{ rad m}^{-1}$ .

increase of winding angle and the generated gaps. Besides, the increase of winding angle also led to the decrease of the contact area between the inner and outer layers of PE fibers. Based on

this fact, we established a simplified model (detailed information is given in the Supporting Information), as presented in Figure 4d–f, that two layers of continuous PE fiber wind around

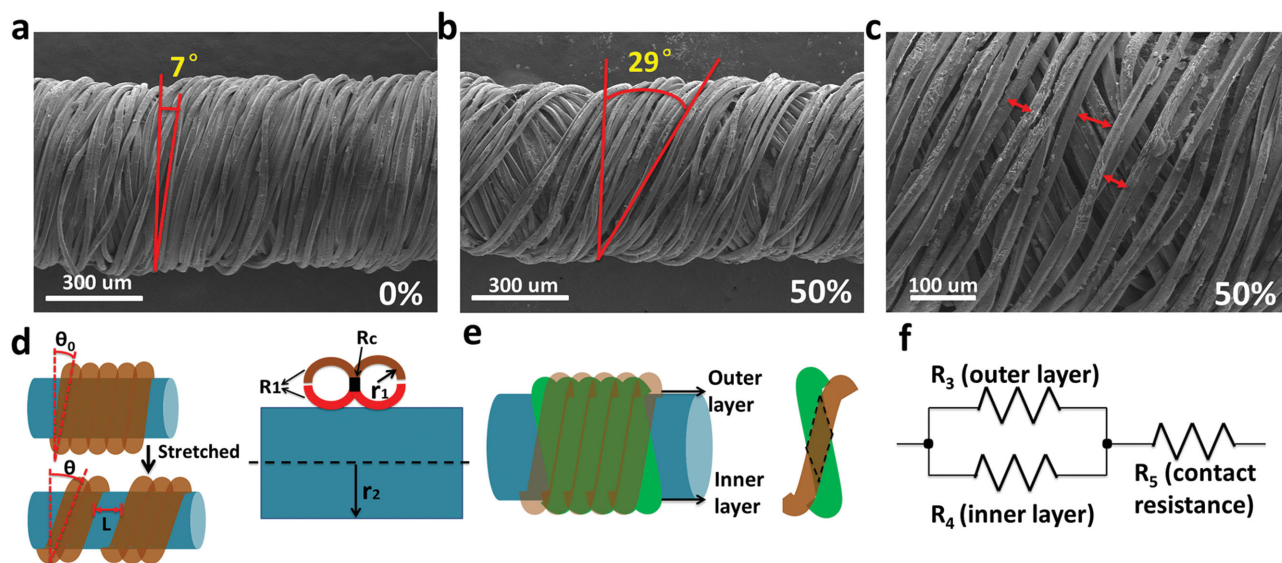


**Figure 4.** Modeling of the mechanism in strain sensing. a) SEM image of PDCY-RGO at 0% strain. The initial winding angle was marked to be  $7^\circ$ . b) SEM image of PDCY-RGO at 50% strain. The winding angle was marked to be  $29^\circ$ . c) SEM image of PDCY-RGO at 50% strain, focusing on localized PE fibers. The generated gaps in-between PE fibers are marked by red double-headed arrows. d) Schematic illustration of the modeling structure. Left: Microstructure variation of PDCY-RGO after being stretched. Right: The longitudinal section diagram of the PDCY-RGO structure. e) Left: The schematic drawing of the doubled covered structure of PDCY-RGO. The green and brown layers represent the inner and outer layers. Right: The overlapping of an inner and an outer PE fiber. The contact area is marked by a black dotted line. f) The resistance model of the overall PDCY-RGO.  $R_3$  and  $R_4$  represent the resistance of the outer and inner covered layers.  $R_5$  referred to the contact resistance between the inner and outer layers.

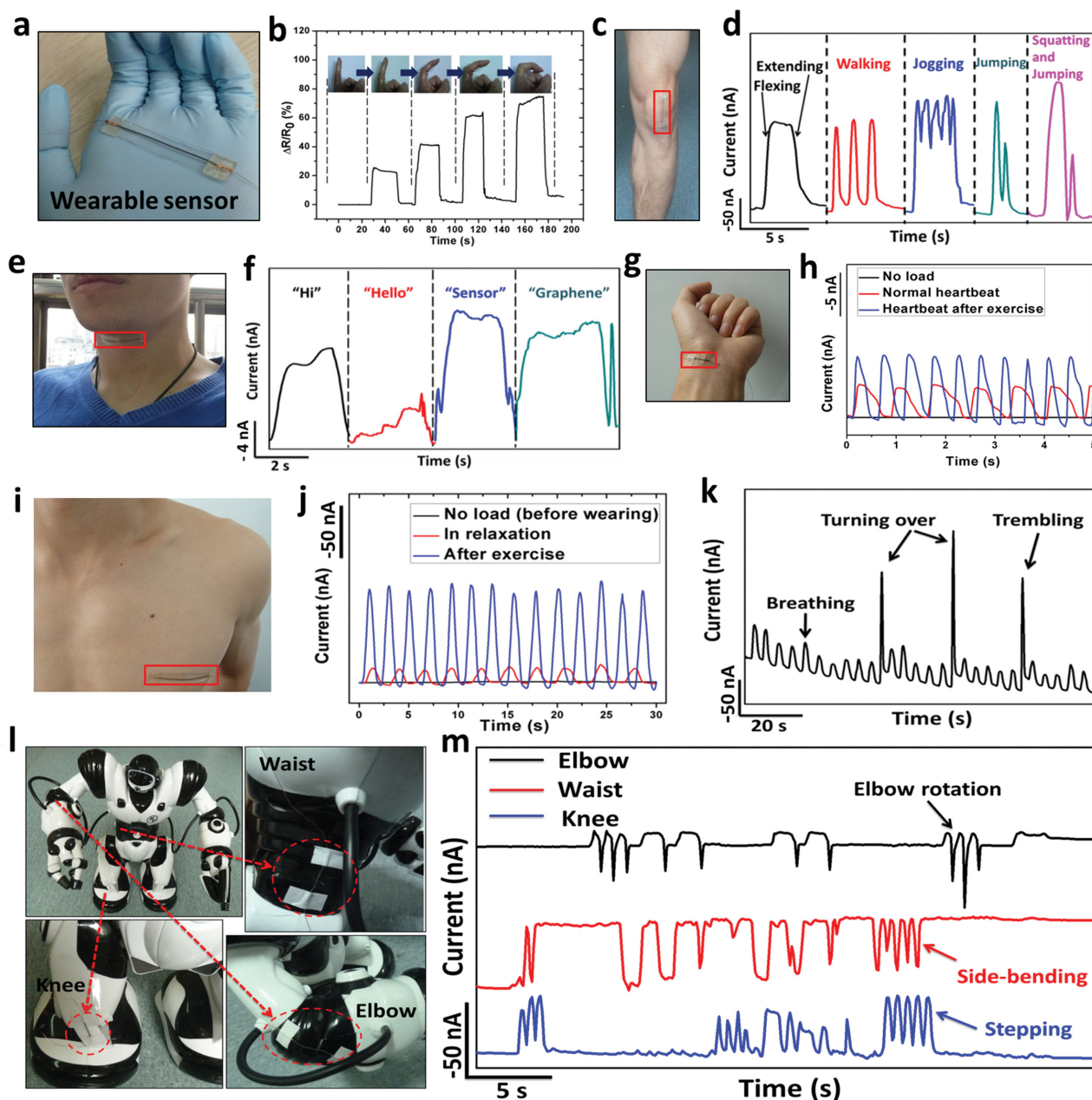


**Figure 5.** Applications as wearable sensors for human and robotics. a) Photograph of the wearable sensor. b) Response signal of wearable sensor in monitoring finger bending. Inset: Photographs of finger-bending to the corresponding positions. c) Wearable sensor attached to the knee, marked in the red box. d) Responsive curves of wearable sensor on the knee under motions of flexing/extending, walking, jogging, jumping, and squatting-jumping. e) Wearable sensor attached to the throat, marked in the red box. f) Responsive curves when wearer spoke "Hi", "Hello", "Sensor", and "Graphene". g) Wearable sensor attached to the wrist, marked in the red box. h) Responsive curves of wearable sensor on the wrist before wearing (no load), and under normal/exercise conditions. i) Wearable sensor attached to the chest, marked in the red box. j) Responsive curves of wearable sensor on the chest before wearing, in relaxation, and after exercise. k) Responsive curves of wearable sensor on the chest. The wearer simulates deep sleep (keeping still) and light sleep (turning over and trembling frequently). l) The robot wears fiber sensors at movable joints (elbow, waist, and knee). Each sensor is marked in the red box at specific joint position. m) Responsive curves of wearable sensors during the robot's dance "Gangnam Style": elbow (black line), waist (red line), and knee (blue line).

a PU core fiber at an initial winding angle of  $\theta_0$ , like a "compression spring." After being stretched to strain of  $\varepsilon$ , gaps emerged in-between the adjacent PE fibers (Figure 4c). As a consequence, in the longitudinal direction of graphene-based fiber, the contact resistance  $R_c$  across two neighboring winding PE fiber was

replaced by the resistance  $R_2$ , along a single PE fiber longitudinally by one circle (Figure 4d), which caused resistance increase of the outer ( $R_3$ ) and inner ( $R_4$ ) layers separately. At the same time, the decrease of the contact area increased the contact resistance ( $R_5$ ) between the inner and outer layers (Figure 4e).

The total resistance model was simplified as in Figure 4f. The resistances of inner and outer layers were in parallel, connected with the contact resistance in series. The relative resistance variation could be determined as Equation (1):

$$\frac{\Delta R}{R_0} = \frac{n \left( \frac{\rho r_2}{t r_1} - R_c \right) + 2 R_a \left( \frac{\sin 2\theta}{\sin 2\theta_0} - 1 \right)}{2 R_a + N \left( \frac{\rho r_1}{4 t r_2} + R_c \right)} \quad (1)$$

Here  $r_1$  and  $r_2$  are the radii of PE fibers and PU fiber, respectively,  $\rho$  and  $t$  are the resistivity and thickness of the RGO sheet,  $\theta$  is the winding angle.  $R_a$  is the initial contact resistance between the inner and outer layers. During the stretch, we could reasonably assume  $r_1$ ,  $r_2$ ,  $\rho$ ,  $t$ ,  $R_c$ , and  $R_a$  are constant. The number of PE fiber windings  $N$  and the generated gap number  $n$  satisfy the relation:

$$\frac{n}{N} = \frac{2 r_1}{L} \cdot \left( \frac{1 + \varepsilon}{\cos \theta_0} - \frac{1}{\cos \theta} \right) \quad (2)$$

From the above analysis, we concluded that the relative resistance variation mainly depended on the gap number  $n$  generated in the PE fiber winding number  $N$ . Equation (2) indicates that  $n/N$  could be acquired from the determination of  $\theta$  and  $L$  (the averaged gap size) at different strains through experimental observation (Figure S22 and Table S6, Supporting Information).

To demonstrate the great potential of graphene-based fibers as wearable sensors for full-range detection of human activities, we assembled the fiber sensors onto an ultrathin PDMS substrate. The wearable sensors could be attached conformally to different positions of human body using medical tapes and the restriction to skin/body motion was minimal as the device was ultra-lightweight (ca. 0.3 g cm<sup>-1</sup>) and highly flexible (Figure 5a). In vigorous motion sensing, the wearable sensors were fixed onto the knuckle (inset in Figure 5b) and knee (Figure 5c). Figure 5b showed the racing of finger-bending (the finger bended with increasing magnitude each time; inset in Figure 5b). In Figure 5d, the sensor easily recorded and discriminated various knee-related motions including knee flexing/extending, walking, jogging, jumping, and squatting-jumping (Movie S1, Supporting Information), by virtue of the distinctly differentiated patterns of response curves. For subtle physiological signal capturing, we attached the wearable sensors to the throat, wrist, and chest (Figure 5e,g,i). In Figure 5f, when the wearer spoke different words, such as “Hi”, “Hello”, “Sensor”, and “Graphene”, the response curves exhibited remarkably characterized patterns with good repeatability (Figure S23, Supporting Information), mainly resulting from the complicated epidermis/muscle movements around throat during phonation. There are very limited reports of wearable sensors capable of specific phonation recognition, which hold potential in applications such as aiding in speech rehabilitation training and human-machine interaction.<sup>[9,21,35]</sup> Wrist pulse is a key physiological signal for determining arterial blood pressure and heart rate. Figure 5h recorded current signal within 5 s before wearing (no load), and under normal/exercise

conditions. The amplitude and frequency of pulse could be read out readily in real time (each peak denotes one pulse). Respiration, another vital signal, was also presented in Figure 5j, allowing for the real-time monitoring of respiration rate and depth in relaxation and after exercise. This could be exploited as early warning systems for sudden infant death syndrome<sup>[36]</sup> and sleep apnea in adults. More interestingly, the sensor on the chest was able to discriminate the turning over and trembling of the wearer from the normal respiration signal based on the magnitude of the signal peaks (Figure 5k and Movie S2, Supporting Information), thus achieving the goal of sleep quality evaluation to some extent.

In addition to wearable sensing for humans, the graphene-based sensor implemented real-time monitoring of complicated movement combination in robotics. Graphene-based fibers were directly fixed across the movable joints (elbow, waist, knee) using adhesive tape (Figure 5l) to detect various kinds of motion, such as elbow rotation, waist side-bending, and stepping, by taking full advantage of the fiber's capability to sense multiple forms of deformation. As a demonstration, we accomplished the real-time detection of the complete set of movements during the robot dancing “Gangnam Style” (Figure 5m and Movie S3, Supporting Information).

In summary, we present a graphene-based fiber, which possesses the combination of high sensitivity and broad workable range in strain sensing, and the capability of detecting multiple deformation forms including tensile strain, bending, and torsion. Another highlight is the facile, low-cost, scalable, and solution-processable fabricating strategy, setting the stage for the practical and widespread utilization as wearable sensors. The underlying mechanism in strain sensing is illuminated by modeling of a “compression spring” structure. The versatile fabrication strategy and unique architecture could be extended to other materials for functionalized composite fibers with superb stretchability.

## Experimental Section

**Fabrication Process of the Graphene-Based Fiber:** DCY (≈650 μm in diameter) yarns are commercially available. The DCY yarns were first cleaned ultrasonically in deionized water for 30 min. After drying in air, DCY were treated by glow discharge plasma (air plasma, 60 Pa, 100 W, 5 min). Ripple-like texture (feature size of ≈70 nm) was generated on PE fiber (≈20 μm in diameter) surface. Then DCY were dip-coated directly in GO dispersion (1.4 mg g<sup>-1</sup> in water) for specific times (2 s for each dip-coating). GO coated on to PE fibers with ease, accompanied by a color change from white to yellowish. Lastly the PDCY-GO was soaked (100 °C, 30 s) in HI acid (57 wt%) to obtain PDCY-RGO, accompanied by an immediate color change from yellowish to black. The PDCY-RGO were rinsed with ethanol for several times and subsequently dried in an oven at 100 °C for 10 min to remove the residual HI acid.

**Integration of the Graphene-Based Fiber into Bending Sensor:** Copper wires (2 μm in diameter) were connected to the two ends of the graphene-based fiber as external electrodes with the help of conductive copper tape and silver paste. Then the graphene-based fiber (4 cm in length) was put on to a PDMS (a 10:1 mixture of the PDMS prepolymer and curing agent, Sylgrad-184, Dow Corning) slab (60 mm × 10 mm × 3 mm). The two ends of the fiber were fixed onto PDMS by dripping a small drop of liquid PDMS and curing (80 °C, 30 min). Lastly adhesive tape was used to attach the two ends of the graphene-based fiber to PDMS slab as a further fixation.

**Integration of the Graphene-Based Fiber into Wearable Sensor:** The procedures to assemble graphene-based fibers into wearable sensors



were basically similar to the integration of bending sensor, except that the PDMS substrate was much thinner (0.4 mm in thickness, 8 mm in width, varying length according to target wearing positions) and the fibers were directly fixed onto the PDMS with medical tape. Then the wearable sensors were attached onto target positions of body with medical tape at the two ends of PDMS to avoid skin irritation. The length of fiber sensors attached to the knuckle, knee, throat, wrist, and chest was 2, 4, 3, 2, and 4 cm, respectively.

**Characterization:** The SEM characterization was accomplished using a Hitachi SU8200 FE-SEM. The micro-Raman testing was performed with a DXR Raman Microscope (Thermal Scientific Corporation, USA, with a 532 nm excitation length). The conductivity of PDCY-RGO with varying dip-coating times was calculated from a modified two-point probe method (Supporting Information). The stress versus strain properties (DCY, PDCY-RGO) were measured with a high-precision electronic universal testing machine (CMT6103, MTS Systems (China) Co., Ltd.). In the testing of strain sensing, the strain loading was implemented with a high-precision motorized linear stage (displacement resolution of 2.5  $\mu\text{m}$ ). In the testing of bending sensing, the universal testing machine (CMT6103, MTS Systems (China) Co., Ltd.) was utilized to bend the sensor to specific position, and the bending angle was determined through angle analysis software from the real-time photographs. To determine the detection limit of bending angle, the device was stretched gradually from a relatively large bending angle (11.0°) and collected the response signal under a series of gradually decreasing step bending angle (Figure S14, Supporting Information). In the testing of torsion sensing, the torsion loading was applied with a high-precision motorized rotation stage (0.0025°). To obtain the resistance variation, a constant voltage (5 V) was loaded on the fiber sensors to acquire a real-time current signal, using an electrochemical workstation (PARSTAT 2273, Princeton Applied Research).

## Supporting Information

Supporting Information is available from the Wiley Online Library or from the author.

## Acknowledgements

This work was financially supported by the National Basic Research Program of China (Grant No. 2012CB932303), the National Natural Science Foundation of China (Grant No. 61301036), Shanghai Municipal Natural Science Foundation (Grant Nos. 13ZR1463600 and 13XD1403900), and the Innovation Project of Shanghai Institute of Ceramics.

Received: July 22, 2015

Revised: August 20, 2015

Published online:

- [1] D. J. Lipomi, M. Vosgueritchian, B. C. K. Tee, S. L. Hellstrom, J. A. Lee, C. H. Fox, Z. Bao, *Nat. Nanotechnol.* **2011**, 6, 788.
- [2] D. H. Kim, N. Lu, R. Ma, Y. S. Kim, R. H. Kim, S. Wang, J. Wu, S. M. Won, H. Tao, A. Islam, K. J. Yu, T. I. Kim, R. Chowdhury, M. Ying, L. Xu, M. Li, H. J. Chung, H. Keum, M. McCormick, P. Liu, Y. W. Zhang, F. G. Omenetto, Y. Huang, T. Coleman, J. A. Rogers, *Science* **2011**, 333, 838.
- [3] T. Yamada, Y. Hayamizu, Y. Yamamoto, Y. Yomogida, A. I. Najafabadi, D. N. Futaba, K. Hata, *Nat. Nanotechnol.* **2011**, 6, 296.
- [4] B. C. Tee, C. Wang, R. Allen, Z. Bao, *Nat. Nanotechnol.* **2012**, 7, 825.
- [5] C. Pang, G. Y. Lee, T. I. Kim, S. M. Kim, H. N. Kim, S. H. Ahn, K. Y. Suh, *Nat. Mater.* **2012**, 11, 795.
- [6] L. Cai, L. Song, P. Luan, Q. Zhang, N. Zhang, Q. Gao, D. Zhao, X. Zhang, M. Tu, F. Yang, W. Zhou, Q. Fan, J. Luo, W. Zhou, P. M. Ajayan, S. Xie, *Sci. Rep.* **2013**, 3, 3048.
- [7] S. Jung, J. Lee, T. Hyeon, M. Lee, D. H. Kim, *Adv. Mater.* **2014**, 26, 6329.
- [8] S. Gong, W. Schwalb, Y. Wang, Y. Chen, Y. Tang, J. Si, B. Shirinzadeh, W. Cheng, *Nat. Commun.* **2014**, 5, 3132.
- [9] D. Kang, P. V. Pikhitsa, Y. W. Choi, C. Lee, S. S. Shin, L. Piao, B. Park, K.-Y. Suh, T.-i. Kim, M. Choi, *Nature* **2014**, 516, 222.
- [10] J. Kim, M. Lee, H. J. Shim, R. Ghaffari, H. R. Cho, D. Son, Y. H. Jung, M. Soh, C. Choi, S. Jung, K. Chu, D. Jeon, S. T. Lee, J. H. Kim, S. H. Choi, T. Hyeon, D. H. Kim, *Nat. Commun.* **2014**, 5, 5747.
- [11] A. Ajovalasit, B. Zuccarello, *J. Strain Anal. Eng.* **2005**, 40, 643.
- [12] A. A. Barlian, W. T. Park, J. R. Mallon Jr., A. J. Rastegar, B. L. Pruitt, *Proc. IEEE* **2009**, 97, 513.
- [13] D. J. Cohen, D. Mitra, K. Peterson, M. M. Maharbiz, *Nano Lett.* **2012**, 12, 1821.
- [14] S. Li, J. G. Park, S. Wang, R. Liang, C. Zhang, B. Wang, *Carbon* **2014**, 73, 303.
- [15] M. Hempel, D. Nezich, J. Kong, M. Hofmann, *Nano Lett.* **2012**, 12, 5714.
- [16] X. Li, R. Zhang, W. Yu, K. Wang, J. Wei, D. Wu, A. Cao, Z. Li, Y. Cheng, Q. Zheng, R. S. Ruoff, H. Zhu, *Sci. Rep.* **2012**, 2, 870.
- [17] C. Yan, J. Wang, W. Kang, M. Cui, X. Wang, C. Y. Foo, K. J. Chee, P. S. Lee, *Adv. Mater.* **2013**, 26, 2022.
- [18] C. S. Boland, U. Khan, C. Backes, A. O'Neill, J. McCauley, S. Duane, R. Shanker, Y. Liu, I. Jurewicz, A. B. Dalton, J. N. Coleman, *ACS Nano* **2014**, 8, 8819.
- [19] J. J. Park, W. J. Hyun, S. C. Mun, Y. T. Park, O. O. Park, *ACS Appl. Mater. Interfaces* **2015**, 7, 6317.
- [20] R. Xu, Y. Lu, C. Jiang, J. Chen, P. Mao, G. Gao, L. Zhang, S. Wu, *ACS Appl. Mater. Interfaces* **2014**, 6, 13455.
- [21] Y. Wang, L. Wang, T. Yang, X. Li, X. Zang, M. Zhu, K. Wang, D. Wu, H. Zhu, *Adv. Funct. Mater.* **2014**, 24, 4666.
- [22] A. P. A. Raju, A. Lewis, B. Derby, R. J. Young, I. A. Kinloch, R. Zan, K. S. Novoselov, *Adv. Funct. Mater.* **2014**, 24, 2865.
- [23] S. Lim, D. Son, J. Kim, Y. B. Lee, J.-K. Song, S. Choi, D. J. Lee, J. H. Kim, M. Lee, T. Hyeon, D.-H. Kim, *Adv. Funct. Mater.* **2015**, 25, 375.
- [24] M. Amjadi, A. Pichitpajongkit, S. Lee, S. Ryu, I. Park, *ACS Nano* **2014**, 8, 5154.
- [25] S. Yao, Y. Zhu, *Nanoscale* **2014**, 6, 2345.
- [26] L. Yang, J. Chen, Y. Guo, Z. Zhang, *Appl. Surf. Sci.* **2009**, 255, 4446.
- [27] W. S. Hummers, R. E. Offeman, *J. Am. Chem. Soc.* **1958**, 80, 1339.
- [28] S. Pei, J. Zhao, J. Du, W. Ren, H.-M. Cheng, *Carbon* **2010**, 48, 4466.
- [29] A. C. Ferrari, J. Robertson, *Phys. Rev. B* **2000**, 61, 14095.
- [30] C. Mattmann, F. Clemens, G. Tröster, *Sensors* **2008**, 8, 3719.
- [31] J. Foroughi, G. M. Spinks, G. G. Wallace, J. Oh, M. E. Kozlov, S. Fang, T. Mirfakhrai, J. D. Madden, M. K. Shin, S. J. Kim, R. H. Baughman, *Science* **2011**, 334, 494.
- [32] L. Shi, T. Zhu, Y.-e. Fan, K. S. Chiang, Y. Rao, *Opt. Commun.* **2011**, 284, 5299.
- [33] T. Yamada, Y. Yamamoto, Y. Hayamizu, A. Sekiguchi, H. Tanaka, K. Kobashi, D. N. Futaba, K. Hata, *ACS Nano* **2013**, 7, 3177.
- [34] T. Yang, Y. Wang, X. Li, Y. Zhang, X. Li, K. Wang, D. Wu, H. Jin, Z. Li, H. Zhu, *Nanoscale* **2014**, 6, 13053.
- [35] X. Wang, Y. Gu, Z. Xiong, Z. Cui, T. Zhang, *Adv. Mater.* **2014**, 26, 1336.
- [36] P. J. Fleming, R. Gilbert, Y. Azaz, P. J. Berry, P. T. Rudd, A. Stewart, E. Hall, *Br. Med. J.* **1990**, 301, 85.